

PAFRAG Modeling and Experimentation Methodology for Assessing Lethality and Safe Separation Distances of Explosive Fragmentation Ammunitions

Vladimir M. Gold

Abstract The fundamental vision of the US Army Armaments Research, Design and Engineering Center, Picatinny Arsenal is that the fragmentation ammunition has to be safe for the soldier and lethal for the adversaries. PAFRAG (Picatinny Arsenal Fragmentation) is a combined analytical and experimental technique for determining explosive fragmentation ammunition lethality and safe separation distance without costly arena fragmentation tests. PAFRAG methodology integrates high-strain high-strain-rate computer modelling with semi-empirical analytical fragmentation modelling and experimentation, offering warhead designers and ammunition developers more ammunition performance information for less money spent. PAFRAG modelling and experimentation approach provides more detailed and accurate warhead fragmentation data for ammunition safe separation distance analysis, as compared to the traditional fragmentation arena testing approach.

Keywords PAFRAG · Smooth Particle Hydrodynamics · CTH computer program · CALE computer program · Arbitrary lagrangian–eulerian formulation

1 Introduction: Fragmentation of Explosively Driven Shells

The subject of fragmentation of explosively driven shells has long been of interest in the military field and has recently commanded attention in a number of other applications including the design of fragment and blast resistant structures and protective facilities. A review of previous work shows that extensive studies on the subject were performed in the early 1940s. Historically, three names of ground-breaking researchers' stand out: Gurney has been credited for deriving a form of an empirical expression for prediction of fragment velocities as a function of the mass ratio between the explosive and the metal shell [1], Mott has been

V.M. Gold (✉)

U. S. Army ARDEC, Picatinny Arsenal, NJ 07806-5000, USA

e-mail: vladimir.m.gold.civ@mail.mil

© Springer International Publishing AG 2017

M.K. Shukla et al. (eds.), *Energetic Materials*, Challenges and Advances

in Computational Chemistry and Physics 25, DOI 10.1007/978-3-319-59208-4_7

credited for developing statistical models for predicting average fragment sizes and fragment mass distributions [2], and Taylor has been credited for developing models describing expanding shell dynamics and the state of stress at the time of fracture [3]. Most of this work, however, ceased shortly after the World War II and was not resumed until the 1960s.

Before the state-of-the-art high-strain-rate high-strain finite difference computer programs had become available to fragmentation munition designers, for nearly six past decades, modeling of explosive fragmentation munitions had relied for a large degree on analytical methods developed in 1940s, that is on the fragment velocity predictions based on Gurney [1] approximations and on the fragment mass distribution statistics based on Mott [2] and/or Gurney and Sarmousakis [4] fragmentation models. A brief overview of empirical fragmentation models widely used in 1960s and 1970s is given by Hekker and Pasman [5]. Mott's [2] approach to the dynamics of fracture activation has been successfully pursued starting in 1980s by Grady and Kipp resulting in significant advances in a number of dynamic fracture and fragmentation areas [6–9] including the high-velocity impact fragmentation [10, 11], shaped charge jet break-up [12], dynamic fragmentation of metal rings [6, 7, 13], spalling phenomena [14, 15], and rock blasting [16]. The extensive influence of Mott's concepts can be found in many other works including that of Hoggatt and Recht [17] and Wesenberg and Sagartz [18]. A comprehensive review of Mott's fragmentation concepts is given by Grady [19]. A perturbation stability approach to fragmentation of rapidly expanding metal rings is given by Mercier and Molinari [20]. A compilation of analytical techniques for assessment of effectiveness of fragmentation munitions can be found in Weiss [21] and a brief review of fragmentation models can be found in Grady [22]. Recently, there had been a number of reports of applying the state-of-the-art continuum hydrocode analyses to the explosive fragmentation problem utilizing Eulerian, Arbitrary-Lagrangian-Eulerian, Lagrangian, Peridynamics, SPH (Smooth Particle Hydrodynamics), and corpuscular model methods [23–27].

An attempt to apply the state-of-the-art continuum hydrocode analyses to the explosive fragmentation problem had been reported by Wilson et al. [28]. The work was performed employing the CTH computer program [29] with a “code-built-in” Grady–Kipp fragmentation model [11, 30] based on the Poisson statistics and the average fragment sizes as functions of the strain-rates $\dot{\epsilon}$. To validate the model, Wilson et al. [28] compared the CTH code analyses with the experimental data, resulting in a good agreement in the average fragment sizes predictions, although the fragment mass distribution predictions were rather poor, in particular for fragments with masses below 2 grains. Since in many military explosive fragmentation applications including the anti-personnel fragmentation warheads, mines, grenades, and mortars the majority of lethal fragments have masses below 2 grains, an improved computational procedure enabling more accurate modeling and simulation of fragmentation munitions has been required.

A technique for predicting performance of explosive fragmentation munitions presented in this work is based on integrating the CALE computer program [31] with a semi-empirical fragmentation computer model PAFRAG (Picatinny Arsenal

FRAGMENTATION). CALE is a plane two-dimensional and three-dimensional axial symmetric high-rate finite difference computer program based on Arbitrary Lagrangian–Eulerian formulation of the governing equations. The mathematical description of the PAFRAG code is given in sections that follow. The geometries of three example problems considered in this work are shown in Figs. 1 and 11. As shown in Fig. 1, upon initiation of the high-explosive charges, rapid expansion of high-pressure high-velocity detonation products results in high-strain high-strain-rate dilation of the hardened steel shells, which eventually rupture generating a “spray” of high-velocity steel fragments. In the case of the Charge A, the dilation of the steel shell is accompanied by the implosion of the copper shaped charge liner that produces a high-speed metal jet moving along the charge’s axis of symmetry z . In the case of the Charge B, in addition to the explosive charge, the hardened steel shell also encapsulates a tracer and a fuze that occupy significant volume of the munition payload. A threaded connection between the fuse and the fragmenting portion of the hardened steel case was also included into the CALE model. In order to allow a “slippage” along the joint, the threads were modeled with a few rows of computation cells employing ideally-plastic-zero-yield-strength material with the same hydrodynamic response parameters as steel. Following the expansion of the detonation products, the fuze section of the warhead is projected in the negative direction of the z -axis, without contributing to the lethality of the fragment spray. In addition to specification of the problem geometry and initial and boundary conditions, equations of state and constitutive equations for all materials have to be specified before the solution procedure can be initiated. The explosive was modeled using the Jones–Wilkins–Lee–Baker equation of state [32] employing a set of parameters resulting from thermo-chemical equilibrium analyses of detonation products with the JAGUAR code [33, 34] and calibrated with copper cylinder test expansion data. The hydrodynamic responses of the steel shell and the copper liner were modeled using a standard linear polynomial approximation usually employed for metals. The constitutive behavior of these metals was modeled using the Steinberg–Guinan yield-strength model [35] and the von Mises yielding criterion. A standard set of parameters based on measured stress and free-surface vs. time histories from shock wave experiments available from Steinberg et al. [35], Tipton [36], and Steinberg [37] had been employed in the analyses. The principal equations of the Steinberg–Guinan yield-strength model are given here for completeness and are as follows:

$$Y = Y_{0f}(\varepsilon_p) \frac{G(p, T)}{G_0} \quad (1)$$

where

$$Y_{0f}(\varepsilon_p) = Y_0 [1 + \beta(\varepsilon_p + \varepsilon_i)]^m \leq Y_{\max} \quad (1a)$$

and

$$G(p, T) = G_0 \left[1 + \frac{Ap}{\eta^{1/3}} - B(T - 300) \right] \tag{1b}$$

In Eqs. (1a) and (1b) $G(p, T)$ is the shear modulus at pressure p and temperature T , G_0 is the initial shear modulus, Y_0 is the yield strength at the Hugoniot elastic limit, ε_p is the equivalent plastic strain, ε_i is the initial plastic strain, Y_{\max} is the work hardening maximum yield-strength, β and m are work-hardening parameters, η is the compression, and parameters A and B represent dependence of the shear modulus on pressure and temperature, respectively.

Since the extent of dilation of the rapidly expanding steel shell is limited by its strength, at some point the shell ruptures generating a spray of steel fragments moving with trajectories at angles Θ with z -axis. Accordingly, the principal topic of this work is a numerical model for analytical description of parameters of the resulting fragment spray as functions of the “spray” angle Θ . In typical large-scale explosive fragmentation tests (“arena” tests) the tested munitions are positioned at the origin of the reference polar coordinate system and surrounded with series of velocity-measuring screens and fragment-catching witness panels, all at significant distances from the warhead. Accordingly, the fragmentation characteristics are

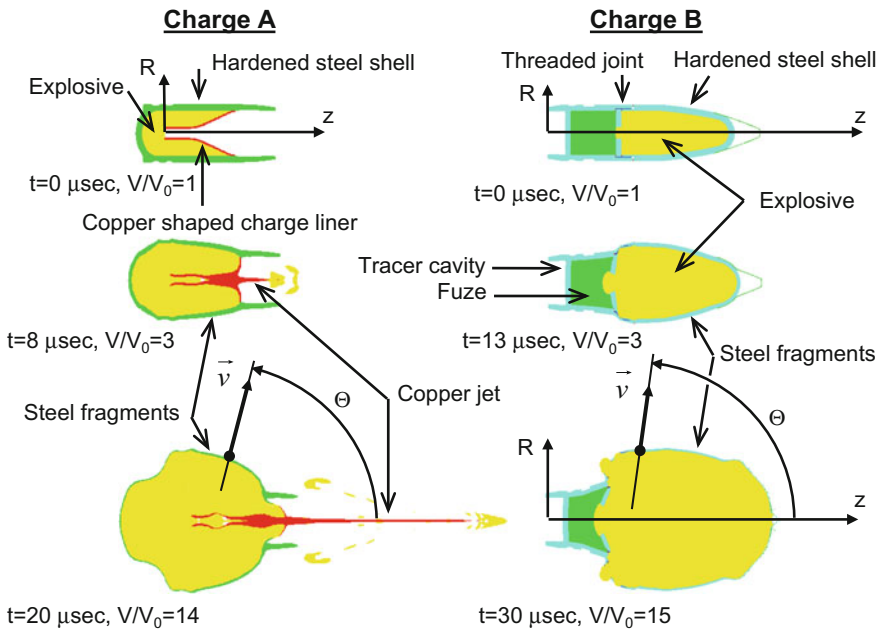


Fig. 1 Results of CALE-code modeling: initial configuration and CALE’s predictions following the explosive detonation initiation

assessed as functions of polar angles Θ' identifying angular positions of these measuring devices.

Initially developed in 2001, for the past decade PAFRAG methodology had been applied in support of tens of US Army ARDEC's explosive fragmentation ammunition design, development, modernization, and characterizations programs resulting in comprehensive collection of PAFRAG code modules, fragmentation warhead analyses, and experimental data. This paper presents a few examples of PAFRAG applications, illustrating utility and versatility of the technique. Since the main objective of the PAFRAG procedure is to simulate the "data output" (i.e. warhead fragmentation performance information) from traditional fragmentation arena tests, a brief description of the fragmentation arena test methodology is given below for completeness.

2 The Fragmentation Arena Test Methodology

Basic principles and requirements governing fragmentation arena test procedures in the U.S.A. are stipulated in Joint Munition Effectiveness Manual [38]. In a typical fragmentation arena test set-up, tested munitions are positioned at the origin of the reference polar coordinate system and surrounded with series of velocity-measuring screens and fragment-catching witness panels, all at significant distances from the warhead. Defining the longitudinal axis of the munition as the polar axis z , the polar altitudinal angles Θ are measured from the munition's nose ($\Theta = 0^\circ$) to the tail ($\Theta = 180^\circ$), and the azimuthal angles ϕ are measured from an arbitrary projectile's feature ($\phi = 0^\circ$) in a counterclockwise direction. In conventional fragmentation arena test procedures fragment sampling and fragment velocity measuring is usually limited to relatively small azimuthal sections, mainly because of enormous construction and data assessment costs associated with recovering fragments from the entire fragmenting shell. This sampling technique requires the assumption of isotropic fragmentation properties for all azimuthal angles ϕ throughout the entire Θ -angle zone, i.e. through a complete altitudinal region bounded by two polar angles. By sampling small azimuthal angles across all polar zones from the munition nose to tail and adjusting this sample data mathematically, a prediction for entire munition fragment characterization is obtained. Since only a small azimuthal section of the region is sampled and scaled up, even relatively small munition positioning errors may result in large deviations of the fragmentation data, routinely requiring repeated testing for statistical data stability.

According to PAFRAG modelling and experimentation methodology, the assessment of the ammunition fragmentation parameters is performed analytically employing the PAFRAG code which links three-dimensional axial symmetric high-strain high-strain-rate continuum analyses with a phenomenological fragmentation model validated through a series of experiments including flash radiography, CelotexTM and water test rear fragments recovery, and sawdust total fragment spray recovery. In fragmentation arena tests, the ammunition

fragmentation characteristics are assessed as functions of polar angles Θ identifying angular positions of fragment-catching witness panels and velocity-measuring screens. In PAFRAG code analyses, positions of these devices are irrelevant, and the fragmentation characteristics are assessed in reference to the fragment trajectory angles Θ' calculated from the CALE code [31] cell velocities at the time of the shell break-up. Once the shell breaks up and fragments are formed, fragment velocities may change with time due to a number of reasons, including the air drag and the rigid body motion induced at the time of the shell break up. Assuming that the fragment trajectory angles Θ do not change with time (that is the rigid body motion and the lateral drift of fragments due to air resistance is relatively small) and that the definitions of angles Θ and Θ' are approximately identical, the PAFRAG model enables prediction of crucial characteristics of explosive fragmenting munitions including the number of fragments, the fragment size distribution, and the average fragment velocities.

3 The PAFRAG Fragmentation Model

Similarly to fragmentation arena test fragment sampling assumptions, the PAFRAG fragmentation model assumes that for any point within a fixed Θ_j -angle zone the fragment number distribution $N_j(m)$ is uniform and independent of the altitude and the azimuth angles Θ and ϕ , respectively. Hence, the total fragment number distribution is given by

$$N(m) = \sum_j^L N_j(m). \quad (2)$$

In Eq. (2) m is the fragment mass, L is the number of altitudinal Θ_j -angle zones, $0 \leq \Theta \leq \pi$, and $N_j(m)$ is the fragment number distribution function for the j -th zone. For convenience, all Θ -zones are assumed to have the same altitudinal lengths of $\Delta\Theta = \pi/(L - 1)$, except for the first and the last “half-length” zones with lengths of $\frac{1}{2}\Delta\Theta$. In the fragmentation ammunition arena testing practice adopted at the US Army Armament Research Development and Engineering Center, the number altitudinal zones is usually $L = 37$, resulting in uniform Θ -angle resolution of $\Delta\Theta = 5^\circ$. Accordingly, the Θ -zones are identified by the middle of the zone altitudinal angles Θ_j given by the following series

$$\Theta_j = \begin{cases} 1/4\Delta\Theta, & j = 1, \\ \Delta\Theta(j - 1), & 2 \leq j \leq L - 1, \\ \pi - 1/4\Delta\Theta, & j = L. \end{cases} \quad (3)$$

In the case of traditional fragmentation arena testing, all individual fragment number distribution functions $N_j(m)$ for all polar Θ -zones are determined directly

from the test data. The main drawback of this approach is the extremely high testing costs limiting the fragmentation arena testing to final ammunition fragmentation characterization. Alternatively, the PAFRAG modeling and experimentation is a relatively low-cost procedure enabling accurate assessment of the fragmenting munition performance at the research, design, and development phases. According to the PAFRAG approach the individual Θ -zone fragment number distribution functions $N_j(m)$ are computed analytically from the sawdust or water tank fragment recovery test data, $N(m)$. Mathematically, the PAFRAG fragmentation modeling is a solution of the inverse problem of Eq. (1), i.e. determining a series of individual $N_j(m)$'s for given $N(m)$. Since with PAFRAG approach, the $N(m)$ function is assessed based on approximately 98–99% fragment recovery data, the accuracy of PAFRAG predictions is high.

PAFRAG code is capable of modeling fragmentation of “natural” and “controlled”, or “pre-formed” fragmentation warheads. In PAFRAG, natural fragmentation warheads are usually modeled using the PAFRAG-MOTT model, “controlled” or “pre-formed” fragmentation warheads are usually modeled using the PAFRAG-FGS2 model. The PAFRAG-MOTT natural fragmentation model is based on Mott’s theory of break-up of cylindrical “ring-bombs” [39], in which the average length of the resulting circumferential fragments is a function of the radius and velocity of the ring at the moment of break-up, and the mechanical properties of the metal. Accordingly, in the PAFRAG-MOTT model the “random variations” in fragment sizes of natural fragmentation warheads are accounted through the following fragment distribution relationship

$$N(m) = \sum_j^L N_{0j} e^{-(m/\mu_j)^{1/2}}. \tag{4}$$

In Eq. (4) N_{0j} and μ_j represent number of fragments and one half of the average fragment mass in the j -th Θ -zone, respectively, computed from the CALE-code data.

The PAFRAG-FGS2 fragmentation model based on Ferguson’s multivariable curve representation [40] and is defined in parametric form as

$$\begin{bmatrix} N_k(\xi_k) \\ m_k(\xi_k) \end{bmatrix} = \begin{bmatrix} \sum_j^L \frac{m_j}{\sum_j^L m_j} (a_{N0k} + a_{N1k} \xi_k + a_{N2k} \xi_k^2 + a_{N3k} \xi_k^3) \\ a_{m0k} + a_{m1k} \xi_k + a_{m2k} \xi_k^2 + a_{m3k} \xi_k^3 \end{bmatrix}. \tag{5}$$

In Eq. (5) ξ_k is a non-dimensional parameter, $0 \leq \xi_k \leq 1$, k is the curve index, $k = 0, 1$, and sixteen coefficients a_N 's and a_m 's are obtained by fitting two curve segments $k = 0$ and $k = 1$ with conditions of curve and tangent continuity at the adjacent ends. More detailed description and application examples for the PAFRAG-MOTT and PAFRAG-FGS2 models are given in sections that follow.

4 The PAFRAG-Mott Fragmentation Model

For a large part the PAFRAG-MOTT fragmentation model is based on the Mott’s theory of break-up of cylindrical “ring-bombs” [39], in which the average length of the resulting circumferential fragments is a function of the radius and velocity of the ring at the moment of break-up, and the mechanical properties of the metal. A brief review of the Mott’s theory is given here for completeness. Following Mott and Linfoot [19], the “random variations” in fragment sizes are accounted through the following fragment distribution relationship

$$N(m) = N_0 e^{-(m/\mu)^{1/2}} \tag{6}$$

In Eq. (6) $N(m)$ represents total number of fragments of mass greater than m , μ is defined as one half of the average fragment mass, $N_0 = M/\mu$, and M is the total mass of the fragments.

In attempting to evaluate the distribution of fragment sizes occurring in the dynamic fragmentation of expanding metal rings, Mott [39] introduced an idealized model in which the average circumferential fragment lengths are not random but determined by the interaction of stress release waves originating from instantaneous fractures in the body. A schematic of the Mott’s model is shown in Fig. 2a. Assuming that a fracture in the ring is supposed to have occurred first at A_1 and that stress release waves have traveled to points B_1 and \underline{B}_1 , further fractures can no longer take place in regions A_1B_1 and $\underline{A}_1\underline{B}_1$. On the other hand, in the regions B_1B_2 and $\underline{B}_1\underline{B}_2$ the plastic strain is increasing, which increases the probability of fractures at any point in these regions, especially at points near B_1 , B_2 , \underline{B}_1 , and \underline{B}_2 . Thus, according to Mott’s theory the average size of fragments is determined by the rate at

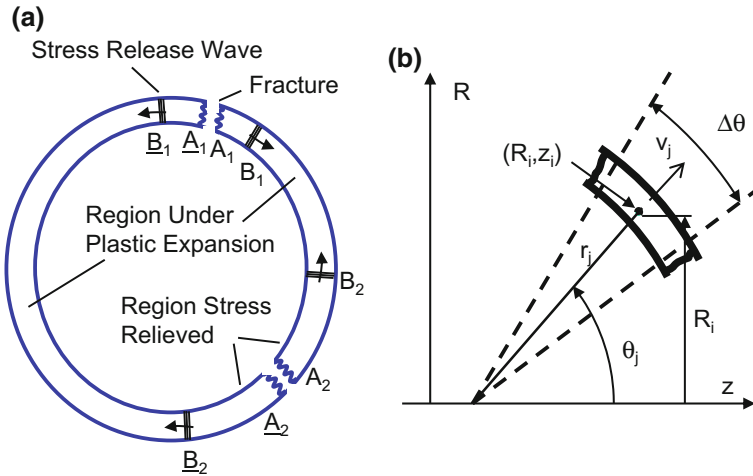


Fig. 2 The fragmentation model schematic

which stress relieved regions A_1B_1 and $\underline{A}_1\underline{B}_1$ spread through the plastically expanding ring.

At the moment of fracture, let r be the radius of the ring and V be the velocity with which the shell is moving outwards. Then, according to Mott [39], the average circumferential length of the resulting fragments is

$$x_0 = \left(\frac{2\sigma_F}{\rho\gamma'} \right)^{1/2} \frac{r}{V} \quad (7)$$

In Eq. (7) ρ and σ_F denote the density and the strength, respectively; and γ' is a semi-empirical statistical constant determining the dynamic fracture properties of the material.

As the shell expands radially, a series of radial fractures propagate along the length of the shell resulting in formation of relatively long splinter-like fragments that continue to stretch in the axial direction. Since the extent of the plastic deformation is limited by the shell strength, the splinter-like fragments eventually break-up forming rugged shaped but approximately proportionally sized prism-shaped fragments. According to Mott [2], the ratios of the fragments' circumferential breadths and the lengths are approximately constant and the average cross-sectional areas are approximately proportional to

$$(r/V)^2 \quad (8)$$

Given that the rugged-shaped fragments can be idealized with simple geometric shapes such as parallelepipeds [2, 22] having longitudinal length l_0 , breadth x_0 , and thickness t_0 , the average fragment mass takes the following form

$$\mu = \frac{1}{2} \alpha \rho x_0^3 \quad (9)$$

In Eq. (9), $\alpha = \frac{l_0}{x_0} \cdot \frac{t_0}{x_0}$. Substituting Eq. (7) into Eq. (9) results in

$$\mu = \frac{1}{2} \left(\frac{2\sigma_F}{\rho^{1/3} \alpha^{-2/3} \gamma'} \right)^{3/2} \left(\frac{r}{V} \right)^3 \quad (10)$$

Since the fragment distribution relationship, Eq. (6), warrants knowledge of the average fragment mass but not the shape, introducing

$$\gamma = \alpha^{-2/3} \gamma' \quad (11)$$

Equation (10) can be put in a simpler and more useful form

$$\mu = \frac{1}{2} \left(\frac{2\sigma_F}{\rho^{1/3}\gamma} \right)^{3/2} \left(\frac{r}{V} \right)^3 \quad (12)$$

A schematic for the technique implemented in the PAFRAG-MOTT model is shown in Fig. 2b. For computational purposes the shell is discretized into a finite number of short “ring” segments, N . For each discrete ring element j uniform field variables are assumed. Accordingly, the masses, the velocities and radii of ring segments j are defined by the mass averages of the respective parameters:

$$m_j = \sum_{L_j} m_i \quad (13)$$

$$V_j = \frac{\sum_{L_j} V_i m_i}{m_j} \quad (14)$$

$$r_j = \frac{\sum_{L_j} R_i m_i}{m_j} \cdot \frac{1}{\sin \Theta_j} \quad (15)$$

$$\Theta_j - \frac{\pi}{2N} \leq \Theta_i < \Theta_j + \frac{\pi}{2N} \quad (16)$$

In Eqs. (13) through (16) m_i , V_i , and R_i denote the mass, the velocity, and the radial coordinate of the i -th computational cell from the CALE-code generated data. As shown in Fig. 2b, the shell is discretized into “ring” elements j in terms of Θ -angles and L_j denotes a number of computational cells contained in the j -th “ring” segment. Θ_j denotes the Θ -angle that corresponds to the j -th ring segment given by

$$\Theta_j = \frac{\pi}{2N} \cdot \left(j - \frac{1}{2} \right) \quad (17)$$

For each computational cell i , the velocity V_i and the Θ -angle Θ_i are calculated respectively by

$$V_i = \sqrt{V_{zi}^2 + V_{Ri}^2} \quad (18)$$

and

$$\Theta_i = \arctan \frac{V_{Ri}}{V_{zi}} \quad (19)$$

In Eqs. (18) and (19) V_{zi} , and V_{Ri} denote the axial and the radial velocity components from the CALE-code generated data.

Given that the velocities and the radii of ring segments j are determined through Eqs. (14) and (15), the resulting fragment size distributions in each segment j can be calculated through the following relationships

$$N_j(m) = N_{0j}e^{-(m/\mu_j)1/2} \quad (20)$$

$$\mu_j = \sqrt{\frac{2}{\rho}} \left(\frac{\sigma_F}{\gamma} \right)^{3/2} \left(\frac{r_j}{V_j} \right)^3 \quad (21)$$

$$N_{0j} = \frac{m_j}{\mu_j} \quad (22)$$

As the detonation wave travels along the shell length and the expanding detonation products rupture the shell, in the case of the idealized “long-pipe-bombs”, the break-up radii r_j and the break-up velocities V_j of the individual segments j are approximately the same, regardless of the axial positions of the segments. Accordingly, taking $\mu \approx \mu_j$, the number of fragment distribution relationship is given by the original Mott’s Eq. (6).

However, in the case of conventional explosive fragmentation munitions with shell geometries far from that of the idealized “long-pipe-bombs”, the break-up radii r_j and the break-up velocities V_j vary along the shell length, so that the resulting variance in the average fragment half-weights μ_j of the individual segments j may be rather significant. The existence of significant differences in the average fragment sizes between the cylindrical and the curved portions of the shell had been experimentally confirmed in this work through flash radiography and high-speed photography. Accordingly, the following two fragment distribution relationships are introduced herein. The “shell-averaged” fragment distribution is defined as

$$N(m) = \tilde{N}_0 e^{-(m/\tilde{\mu}_0)1/2} \quad (23)$$

where \tilde{N}_0 and $\tilde{\mu}_0$ are defined as

$$\tilde{N}_0 = \sum_j N_{0j} \quad (24)$$

$$\tilde{\mu}_0 = \frac{\sum_j m_j}{2\tilde{N}_0} \quad (25)$$

The “ring-segment-averaged” fragment distribution is defined as

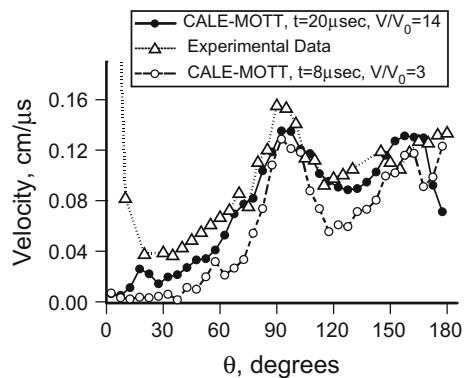
$$N(m) = \sum_j N_{0j} e^{-(m/\mu_j)1/2} \quad (26)$$

5 PAFRAG-Mott Model Validation: Charge a Analyses

The validation of the PAFRAG-MOTT fragmentation model was accomplished using existing *Charge A* arena test data. The fundamental assumption of all fragmentation analyses presented in this work was that the fragmentation occurs simultaneously throughout the entire body of the shell. Following Mott's critical fracture strain concept [39] and assuming that for given shell geometry and materials, the shell fragmentation time is a function of the plastic strain in the shell, the shell fragmentation time can be conveniently expressed in terms of the global shell dilatational properties. Given that in a typical fragmentation munition device the explosive is tightly confined inside the shell, the cumulative strains of the expanding explosive and the surrounding shell are nearly proportional. Accordingly, the critical fracture strain at the moment of the shell break-up may be conveniently measured in terms of the high explosive detonation products volume expansions, V/V_0 .

Figure 3 shows the effect of the shell fragmentation time on the fragment spray velocity distribution function. The seemingly significant disagreement between the experimental velocities and the analyses for $\theta \leq 15^\circ$ is due to deliberate omission of the shaped charge jet data from the PAFRAG-MOTT fragmentation analyses, mainly because of the minimal contribution to the overall fragment-spray lethality. Accordingly, the copper shaped charge jet was neglected in all fragmentation analyses, although included in the CALE model in order to maintain proper explosive confinement parameters. As shown in Fig. 3, varying the shell fragmentation time from approximately $8 \mu\text{s}$ (at which the detonation products had expanded approximately 3 times its original volume, $V/V_0 \sim 3$) to approximately $20 \mu\text{s}$ ($V/V_0 \sim 14$), the resulting changes in the fragment spray angles θ were rather small, while the fragment spray velocities were affected rather significantly. As shown in Fig. 3, delaying the moment of the shell break-up predicts considerable increases in the fragment spray velocities, apparently due to the prolonged "pressurized" interaction with expanding detonation products that increased the total momentum transferred to the shell.

Fig. 3 Fragment velocity distribution versus spray angle θ . Charge A



Figures 4 through 6 show plots of the number of fragments in the fragment spray as functions of the fragment size m/μ , the choice of the number of fragment distribution function model, Eqs. (23) and (26), the spray angle Θ , the shell fragmentation time, and the dynamic fracture parameter γ . As shown in the figures, increases in the parameter γ had resulted in increases of the number of fragments N , both for the $N-m/\mu$ and the $N-\Theta$ relationships. These results are in agreement with the Mott’s theory [39], according to which the parameter γ defines the probability of fracture in the plastically expanding shell determining the number of breaks in the circumferential direction.

Figure 4 shows a plot of a series of curves given by Eq. (23), $N(m) = f_{(23)}(m, \gamma)$, all analyses repeated for two parameters considered: the shell fragmentation time assumed and the dynamic fracture constant, γ . For example, taking the 8μ ($V/V_0 \sim 3.0$) fragmentation time with $\gamma = 12$ and the 20μ ($V/V_0 \sim 14$) fragmentation time with $\gamma = 30$ resulted in nearly identical fragment distribution curves, both in good agreement with the data. The accepted shell fragmentation time had been determined from the high-speed photographic data of Pearson [41] which reasonably agreed with the CALE analyses. Following Pearson [41], the fragmentation of shells with the idealized cylindrical geometries occurs approximately at 3 volume expansions, the instant of fragmentation defined as the time at which the detonation products first appear emanating from the fractures in the shell. In the CALE analyses, the time of shell fragmentation was defined by the structural failure of the shell modeled with the Steinberg-Tipton failure model [31] with the strain work-hardening failure-limit condition $Y = Y_{max}$, Eq. (1a). Once the $Y = Y_{max}$ failure criterion was met, the yield-strength of the “failed” material was set to zero, which provided a reasonable approximation of structural failure of plastically expanding shell. CALE analyses showed that as the detonation wave propagated along the length of the charge and the shell continued to expand radially, the average shell failure strains were in the order of $\epsilon \sim 0.5-0.7$ and at approximately 8μ ($V/V_0 \sim 3.0$) the entire shell had failed. Accordingly, the accepted shell fragmentation time was approximately 8μ ($V/V_0 \sim 3.0$).

Fig. 4 Cumulative number of fragments in the fragment spray versus the fragment size m/μ . Charge A

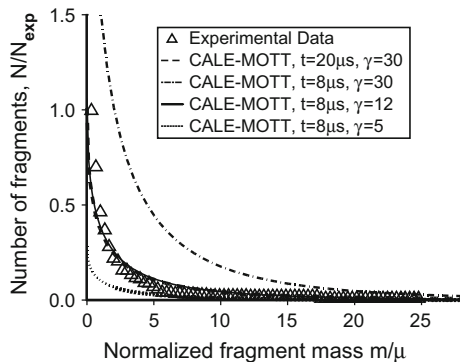


Figure 5 shows a plot of the cumulative number of fragments from the arena test data and the PAFRAG-MOTT analytic predictions employing $N(m) = f_{(23)}(m, \gamma)$ and $N(m) = f_{(26)}(m, \gamma)$ relationships, i.e. the overall “shell-averaged” fragment size distribution, Eq. (23), and the “ring-segment-averaged” fragment size distribution, Eq. (26), respectively. As shown in the plot, employing Eq. (23) resulted in consistently higher values of the cumulative numbers of fragments than that of Eq. (26), apparently because of the nature of the definition of the overall “shell-average” fragment mass $\tilde{\mu}_0$, Eq. (25). As shown in the figure, two equally reasonable fits were obtained for both relationships considered, resulting in $\gamma = 12$ for Eq. (23) and in $\gamma = 14$ for Eq. (26) with the standard deviations of approximately $\sigma_{\gamma=12}(1.62) = 2\%$ and $\sigma_{\gamma=14}(1.62) = -2\%$, respectively. Both curves were fitted at a single point $m_0/\mu = 1.62$, which corresponds to the total number of fragments with mass greater than m_0 ; the aim was to replicate the overall lethality of the fragmenting spray, rather than focusing on the entire range of the m/μ values considered. Accordingly, the accepted shell fragmentation had been approximately $8 \mu s$ ($V/V_0 \sim 3.0$) and two values $\gamma = 12$ and $\gamma = 14$ were selected for all further analyses.

A comparison between empirical values of γ with “theoretical” values of γ' is of interest. According to Mott [39]:

$$\gamma' = 2 \ln(N\tilde{V}) \frac{1}{n} \frac{d(\ln \sigma)}{d\varepsilon} \tag{27}$$

Equation (27) is based on the fundamental assumption that initiation of fractures in plastically expanding metal shells is due to microscopic flaws and cracks normally present in all metals, wherein fractures occur when the maximum principal stress reaches a value large enough to start a crack at the weak point for which the crack length is the largest. In Eq. (27) N represents a number of microscopic flaws

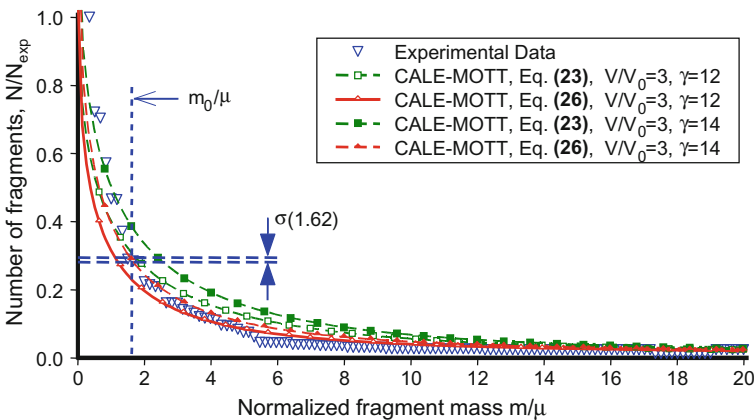


Fig. 5 Cumulative number of fragments versus m/μ for varying γ . CALE-MOTT analyses using Eqs. (19) and (22). Charge A

in a unit volume \tilde{V} , parameter n is an exponent in the relationship between the stress σ at which the crack spreads and the length of the crack, and ε is the strain. Following Taylor [3], at the moment of fracture the circumferential stress at the outer surface of radially expanding ring is $\sigma_{\Theta\Theta} = Y$ and the radial stress is $\sigma_{rr} = 0$. Employing the Steinberg-Guinan yield-strength model, Eq. (1), and assuming that the initial strain in the shell $\varepsilon_i = 0$, and that the shell fractures when the principle strain reaches the value of ε_F , Eq. (27) takes following form:

$$\gamma' = 2 \ln(N\tilde{V}) \frac{1}{n} \frac{m\beta}{1 + \beta\varepsilon_F} \quad (28)$$

Substituting Eq. (28) into Eq. (7) results in:

$$x_0 = \left(\frac{4 \ln(N\tilde{V})}{\rho n} \frac{\sigma_F (1 + \beta\varepsilon_F)}{\beta m} \right)^{1/2} \frac{r}{v} \quad (29)$$

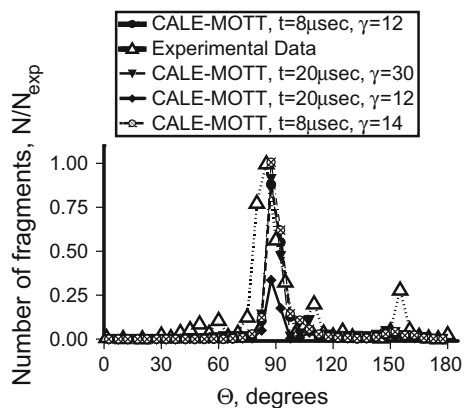
Equations (28) and (29) are useful for examining the relationship between the resulting fragment mass distribution and the principal physical properties of fragmenting metal shells. As evident from Eq. (29), modeling fragmentation of ductile high-strength metals with larger values of fracture stress σ_F and fracture strain ε_F , Mott's theory correctly predicts larger average fragments x_0 and fewer numbers of fragments N . Similarly, modeling high-fragmentation brittle metals with rapid strain hardening rates defined by parameters β and m , Eq. (29) correctly predicts larger numbers of fragments N and smaller average fragments x_0 because of the increased fracture probability γ' , Eq. (28).

Given that for most metals and metal alloys the yield-strength is a function of strain-rate softening and strain hardening, Eqs. (6) and (10) model the number of fragments N and the average fragment mass μ_0 as a function of a ratio σ_F/γ' where fracture stress σ_F corresponds to the yield-strength Y at the time of fracture and fracture constant γ' defines the probability of shell's fracture or "brittleness". Accordingly, in fragmentation analyses, the value of fracture stress σ_F was set to the value $\sigma_F = Y_{\max}$, while values of γ had been obtained by fitting Eqs. (23) and (26) to experimental fragment distribution data. It is interesting to compare the experimental value of γ which includes the average fragment shape coefficient α with a theoretical value of γ' given by Eq. (28). For example, assuming SAE 4340 steel with Rockwell hardness C38 and the initial strain $\varepsilon_i = 0$, from Steinberg [37] values of work-hardening parameters β and m are $\beta = 2$ and $m = 0.5$. Given that at the moment of break-up, $V/V_0 \sim 3.0$, the average fracture strain ε_F in the shell is $\varepsilon_F \approx [(V/V_0)^{1/2} - 1] \sim 0.73$. Following Mott (1947) and assuming Griffith (1924) form of relationship between the stress and the crack length, the parameter $n = 1/2$. Value of N can be only guessed. For example, for N , Mott [39] assumed that average distances between microscopic flaws are approximately in order of $0.1 \mu\text{m}$, hence $NV = 10^{15}$. Assuming $n = 1/2$ and $N\tilde{V} = 10^{15}$ Eq. (28) results in $\gamma' = 56$.

Substituting $\gamma' = 56$ in Eq. (11) results in α from 8 to approximately 10: for $\gamma = 14$, $\alpha \approx 8$; for $\gamma = 12$, $\alpha \approx 10.1$; which is in good agreement with the adopted fragment shape idealization model and with author's observations, although no quantitative assessment of values of α had been attempted. Precise statistical assessment of fragment shapes to obtain averaged values of α is quite laborious and costly, in particular for the state-of-the art high-fragmentation steels producing a large number of small fragments with weights less than 3 grains (0.2 g) which usually represents more than 70% of all "countable" fragments having weights greater than 0.3 grains (0.02 g). For relatively large fragments with weights greater than 5 grains (0.3 g), representative values of average aspect ratios of fragments lengths to circumferential breadth l_0/x_0 are available from the literature. For example, Mott [39] reports that for World War II British Service munitions, $l_0/x_0 \sim 5$, and for World War II German munitions, $l_0/x_0 \sim 2.5$ (Mott, 1943); Mock and Holt [42] report that for Armco iron cylinders, $l_0/x_0 \sim 5$, and for high-fragmentation HF-1 steel cylinders, $l_0/x_0 \sim 2.5$. Accordingly, considering idealized approximately square-shaped base parallelepiped fragments with aspect ratios $l_0/x_0 \approx t_0/x_0$, α (l_0/x_0)², yields for high-fragmentation steel cylinders $\alpha \approx 6.3$, which compares reasonably well with α approximately from 8 to 10 from this work.

Figure 6 shows a plot of the number of fragments with mass greater than 3 grains versus the spray angle Θ , which is the principal lethality parameter of the fragment spray of the munition. The disagreement between the analyses and small spikes at 45° and 60° is probably due to fragments from the shaped charge liner-retaining ring, which had not been included in the CALE model, mainly because of the minimal effect on the overall fragment lethality. The disagreement between the analyses and the spike at 155° is probably due to fragments from a rotating band that had not been included in the CALE model. As shown in the figure, even using a relatively crude assumption of the shell fragmentation time, the overall agreement between the analyses and the experimental data is very good.

Fig. 6 Number of fragments in the fragment spray: varying the shell fragmentation time and the γ . Charge A



6 Charge B Modeling and Experimentation

After having established the crucial parameters of the model, *Charge B* shown in Fig. 1 was designed to maximize the total number of lethal fragments generated. Upon fabrication, the performance of the new charge was tested in a series of experiments including flash radiography, high-speed photography, and sawdust fragment recovery.

The flash radiography tests were performed using two 150 kV x-ray heads located approximately 74 in. in front of the round. Shortly after initiating the round, each of the two x-rays heads were flashed at the separate prescribed times and intervals several microseconds apart. Two flash radiography tests were conducted. Each test resulted in two dynamic images of the expanding fragmented steel shell, both images superimposed on the film.

The high-speed photography tests were performed employing Cordin Framing Camera Model No. 121 capable of recording up to 26 high-speed exposure frames with time intervals between individual frames of less than 1 μ s apart. In the experiments, the round was placed on a test stand in front of a fiducial grid, surrounded with four Argon gas light bombs, all enclosed in a white paper tent. A total of two high-speed photography tests were conducted, each test resulting in over 20 dynamic images of the expanding and fragmenting shell, approximately one microsecond apart.

Figure 7 shows a comparison between the CALE code predictions and the images of the expanding and partially fractured shell obtained from the flash radiography and high-speed photography experiments. The figure shows that the model resulted in an accurate prediction of the shape of the expanding hardened steel shell, including the early break out of the detonation products through the joint between the fuze and the main charge. After the shell breaks up and the detonation products start moving through the air, the discrepancy between the position of the edge of the detonation products cloud observed from the high-speed photography and that from the CALE code simulations is relatively large and needs to be commented. The discrepancy is mainly due to modeling approximations in applying the idealized three-dimensional axisymmetric geometry assumption, the Steinberg-Tipton failure algorithm, and the JWLB equation of state to simulate a complex physical phenomenon of shell fracture coupled with high-rate high-pressure-gradient flow of detonation products through cracks into relatively low pressure regions of air surrounding the shell. Given an excellent overall prediction of the shape of the expanding fragmenting shell evident from flash radiographic images, the final impact of these modeling errors is minimal.

Referring to the flash radiographic image of the partially fragmented shell given in Fig. 7, it is important to note remarkable difference between shapes and sizes of fragments ejected from the cylindrical and the curved portions of the charge. As seen from both the 27 μ s and from the 45 μ s radiographic images, the majority of cracks in the cylindrical portion of the charge are in the axial direction, resulting in fragment spray with relatively large axially oriented splinter-like fragments. On the

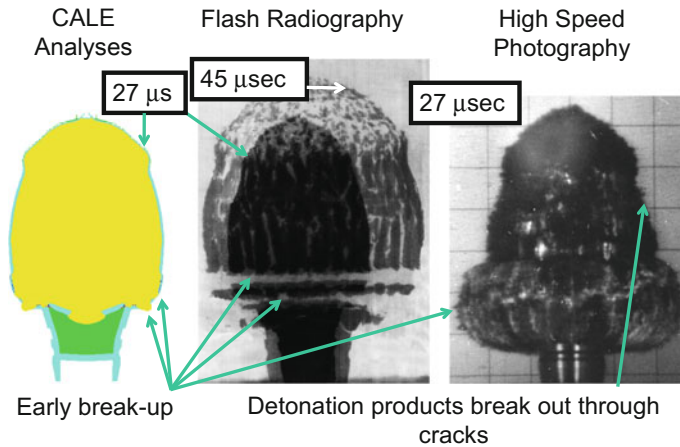


Fig. 7 CALE code modeling and experimentation. Charge B

contrary, in the curved nose portion of the shell, the orientation of cracks is random and distances between fissures are shorter, resulting in fragment spray of predominantly small compactly shaped fragments.

Figure 8 shows a series of high-speed photographic images of the state of the shell's surface as the warhead's hardened steel case expands and the detonation products emerge through cracks. As shown in the figure, visible fractures start to appear on the surface of the shell at approximately $9.4 \mu\text{s}$ after the detonation, which according to the CALE code analyses corresponds to approximately $V/V_0 = 1.8$. Examination of the entire series of images taken approximately one microsecond apart shows that as the shell expands, fractures develop first in the cylindrical portion of the shell. As the shell continues to expand, the developed fractures propagate mostly in the axial direction, occasionally linking-up by new cross-cracks in the circumferential direction, ultimately resulting in formation of large splinter-like fragments shown in the radiographic images of Fig. 7.

As the shell continues to expand, fractures gradually advance towards the curved nosed portion of the shell, and at approximately $19.8 \mu\text{s}$, or at approximately 6.2 volume expansions, the entire shell is fully fragmented, the fragmentation being defined as the instant at which the detonation products first appear as they emanate from the fractures in the shell. Following the PAFRAG-MOTT model assumption that the critical fracture strain at the moment of the shell break-up is expressed in terms of the high explosive detonation products volume expansions, the "average" volume expansion at the time of the shell break-up is then approximately one-half of the value of volume expansions of the fully fragmented shell, hence $V/V_0 = 3.1$. It is interesting to note that the value of $V/V_0 = 3.1$ is in excellent agreement with that assumed initially based on the high-speed photographic data of Pearson [41] for an open ended SAE 1015 steel cylinders filled with Comp C-3 explosive. At a framing rate of 330,000 frames per seconds the recording time was about $75 \mu\text{s}$,

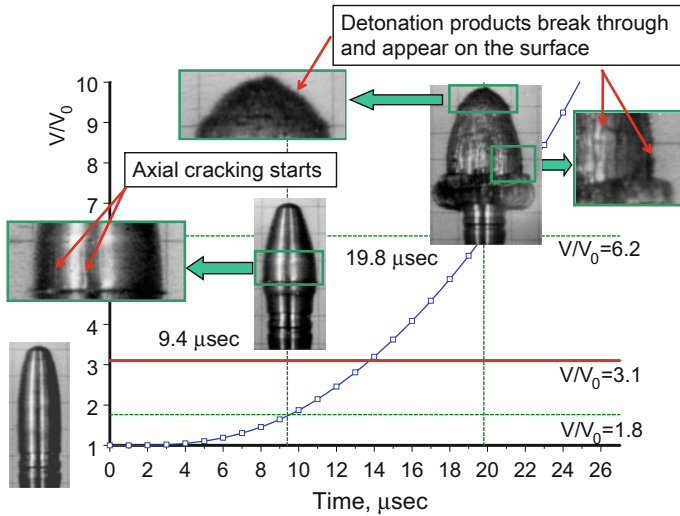
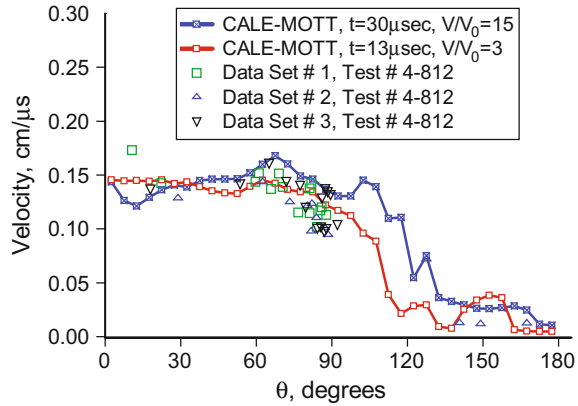


Fig. 8 Development of surface fractures in the expanding shell. Charge B

resulting in approximately the same number of high-speed images as in the this work. It is also interesting to note that changing initial test temperatures from normal 26 °C to -79 °C resulted in significant changes in the fragment cross-sectional shapes from the shear fracture mode to a combination of shear and brittle tensile fracture, but the value of the volume expansion at the time of the shell break-up remained approximately the same. More detailed information regarding the tests can be found in Pearson [41].

Figure 9 shows plots of PAFRAG-MOTT analytic predictions of the fragment velocity distribution function and the experimental data. The experimental data considered here were reduced from the radiographic images of the expanding and partially fractured shell. As shown in the figure, two analytical fragment velocity distribution functions were considered: (i) assuming that the entire shell fragments instantly at approximately at 13 μs ($V/V_0 = 3$), and (ii) assuming that the entire shell fragments instantly at approximately at 30 μs ($V/V_0 = 15$). Given that the explosive was modeled using a semi-empirical set of parameters calibrated with the experimental copper cylinder expansion data, the CALE predictions of the expanding (but not fractured) shell velocities should be reasonably accurate. As shown in the figure, the agreement between the data and the $V/V_0 = 3$ curve is significantly better than with the $V/V_0 = 15$ curve, suggesting that the shell fractured at approximately 3 volume expansions. In addition, given that (according to the high-speed photography) the entire shell had fully fractured at approximately 6.2 volume expansions, the assumption of the $V/V_0 = 3$ instantaneous fracture event is quite reasonable: once the detonation products start to escape through the cracks, any further gains in the velocities are relatively small and may be neglected.

Fig. 9 Fragment velocity distribution versus spray angle θ . Design B



The fragment recovery tests considered in this work were performed employing disposable plastic containers measuring approximately 52 in. in diameter and 59 in. in height, filled with approximately 1000 lbs of sawdust. After inserting the tested round in an inflatable rubber balloon and filling the balloon with air, the balloon was positioned in the sawdust in the middle of the plastic container. After detonating the round, the resulting fragments were recovered employing a combination of the magnetic (for separating fragments from the sawdust) and the vacuum (for separating sawdust from the fragments) recovery techniques. Mass distribution of the collected fragments was analyzed employing an electronic high precision balance gauge interfaced with a computer system capable of automatic counting of fragments as they were manually placed on the scale and weighed. Weighing of the fragments was performed employing the Ohaus Voyager Balance model V14130 gauge with the maximum capacity of 410 g and the precision of 0.001 g. A total of two sawdust recovery tests were performed, each of the tests resulting in successful recovery of approximately over 99.8% of the mass of the steel shell.

Figure 10 shows plots of PAFRAG-MOTT analytic predictions of the cumulative number of fragments compared with the data from the fragment recovery tests. As shown in the figure, two analytic relationships had been considered: (i) the “shell-averaged” fragment size distribution, Eq. (23), and (ii) the “ring-segment-averaged” fragment size distribution, Eq. (26). As shown in the figure, the analytic prediction of Eq. (23) significantly disagrees with the experimental data, regardless of the value γ considered. The disagreement between the Eq. (23) predictions and the data is mostly because of the significant variance in fragment weights μ_j along the shell, ultimately resulting in over-predicting the “shell-averaged” fragment weight $\tilde{\mu}_0$, Eq. (26). On the contrast, the agreement between the data and the $\gamma = 14$ “ring-segment-averaged” fragment size distribution given by the Eq. (26) is quite good: $\sigma_{\gamma=14}(1.051) = -7.3\%$. Given relative simplicity of the model, the overall agreement between the analyses and the data is excellent.

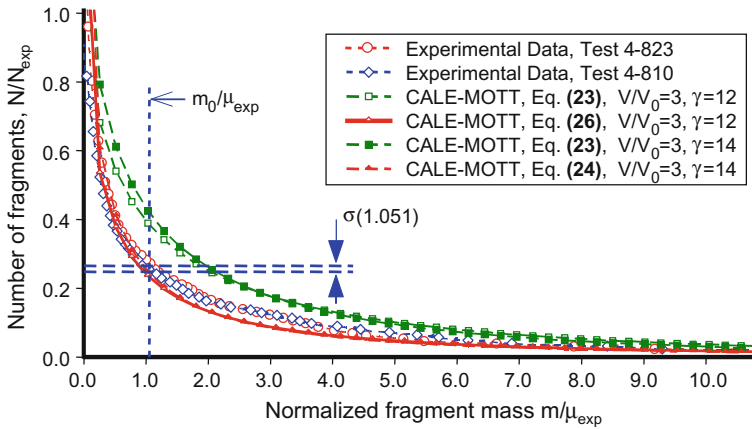


Fig. 10 Cumulative number of fragments versus normalized fragment mass m/μ_{exp} . Charge B

7 Charge C Modeling and Experimentation

Figure 11 shows results of high-strain high-strain-rate CALE modeling and flash radiographic images of a representative natural fragmentation warhead, Charge C, at 30 and 50 μs , and at 300 and 500 μs after detonation. As shown in the figure, upon initiation of the high explosive, rapid expansion of high-pressure high-velocity detonation products results in high-strain high-strain-rate dilation of the hardened fragmenting steel shell, which eventually ruptures generating a “spray” of high-velocity steel fragments. As shown in the Charge C model, the rear end of the warhead has a cylindrical cavity for the projectile tracer material. Following the expansion of the detonation products, the tracer holder fractures and the resulting fragments are projected in the negative direction of the z -axis, without contributing to the warhead lethality but posing potential danger to the gunner. As evidenced from the series of flash radiographic images shown in Fig. 11, the tracer holder section of the warhead breaks up into a number of relatively large fragments that may cause serious or fatal injuries to the gunner.

The Charge C CALE analyses had been conducted until approximately 30 μs after the charge initiation. As shown in the figure, CALE modeling results are in very good agreement with flash radiographic images of the fragmented warhead. As discussed in the previous sections, the fundamental assumption of all fragmentation analyses presented in this work was that the fragmentation occurs simultaneously throughout the entire body of the shell, at approximately at 3 volume expansions, the instant of fragmentation defined as the time at which the detonation products first appear emanating from the fractures in the shell. Accordingly, at approximately 3 volume expansions (12.5 μs), the Charge C fragmenting steel shell was assumed completely fractured, and the CALE-code cell flow field data was passed to PAFRAG-MOTT and PAFRAG-FGS2 fragmentation modeling.

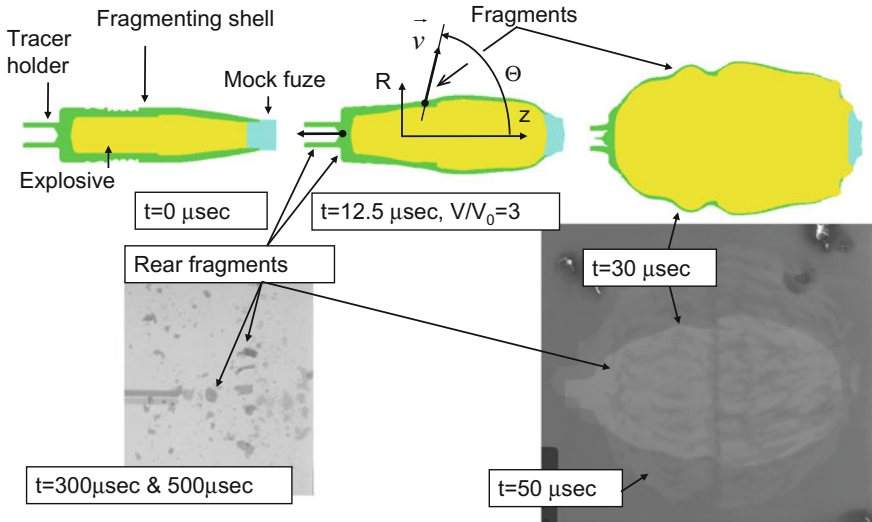


Fig. 11 Results of CALE modeling and flash radiographic images of a natural fragmentation warhead at 30 and 50 μs (test No. X-969), and at 300 and 500 μs (test No. Y-070) after detonation. Charge C

Results of PAFRAG modeling of the Charge C are given in Figs. 12, 13, 14 and 15. Figure 12 shows plots of the cumulative number of fragments versus fragment mass for small-to-moderate weight ($m/\mu_0 < 5.5$) and for relatively large ($m/\mu_0 > 5.5$) fragments calculated with PAFRAG-MOTT and PAFRAG-FGS2 models. As shown in the figure, attempting to fit the sawdust fragment recovery data with the PAFRAG-MOTT model by changing parameter γ “rotated” the curve, but did not yield an accurate fit to the data. Accordingly, more a “flexible” PAFRAG-FGS2 model was applied. As shown in the figure, using the PAFRAG-FGS2 model resulted in accurate fit throughout the entire range of data. Accordingly, PAFRAG-FGS2 model was used for all further Charge C analyses.

Figure 13 shows the PAFRAG model fragment velocity predictions compared with the experimental data. The experimental values of fragment velocities of the main fragment spray ($80^\circ \leq \Theta \leq 100^\circ$) were obtained from the flash radiographic images at 29.4 and 49.9 μs . Velocities of the rear fragments broken off from the tracer section of the shell (which move significantly slower than fragments from the main spray) were assessed from the flash radiographic images at 125.2, 300.0 and 310.9 μs . PAFRAG model prediction of the “average” Θ -zone fragment velocities was obtained from the momentum averaged CALE-code flow field cell velocities. As shown in the figure, the agreement between the PAFRAG model fragment velocities predictions and the data is good.

Figure 14 shows PAFRAG model predictions of the fragment mass distribution versus the spray angle Θ ; the zonal fragment mass m_j and the cumulative fragment mass M distribution functions were computed from CALE-code cell flow field data.

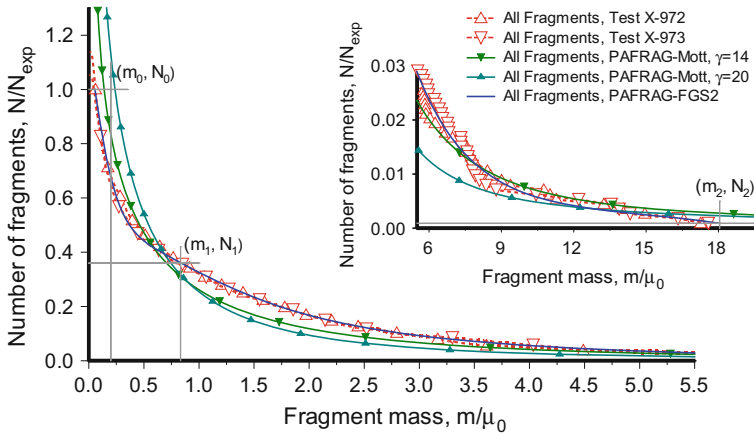


Fig. 12 Cumulative number of fragments versus fragment mass, $N = N(m)$, for small-to-moderate weight ($mlm_0 < 5.5$) and relatively large ($m/m_0 > 5.5$) fragments. Charge C

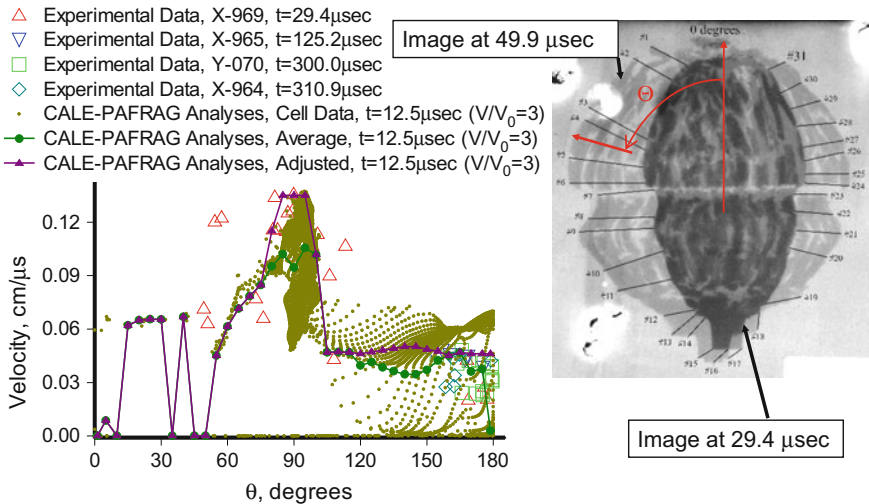


Fig. 13 Fragment velocities versus fragment spray angle Θ and flash radiographic images at 29.4 μs and 49.9 μs (test No. X-969) after detonation. Charge C

For representation clarity, the cumulative fragment mass function M is defined in terms of angle $180^\circ - \Theta$, not the spray angle Θ . As shown in the figure, the PAFRAG model prediction of the cumulative fragment mass distribution M is in good agreement with the available experimental data at $\Theta = 161.6^\circ$ (the Celotex™ and the water test fragment recovery) and at $\Theta = 180^\circ$ (the sawdust fragment recovery).

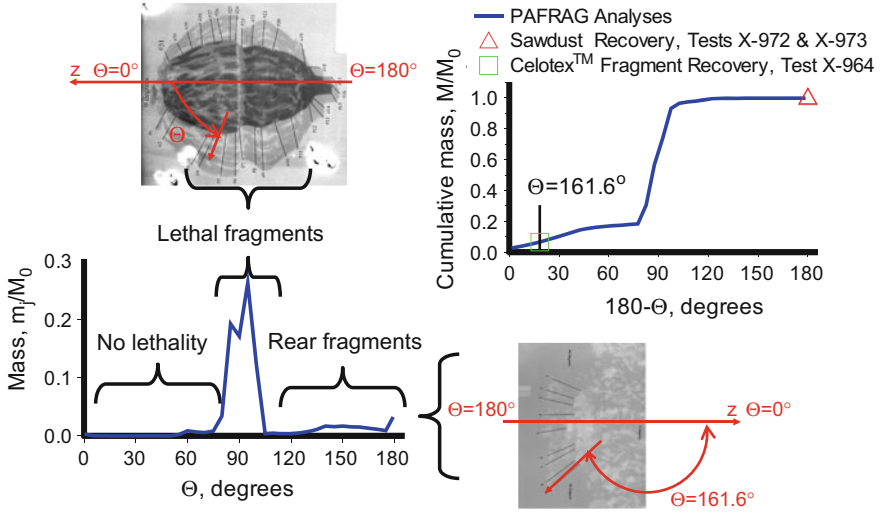


Fig. 14 PAFRAG analyses of fragment mass distribution versus θ . Cumulative fragment mass distribution from PAFRAG analyses is in excellent agreement with experimental data. Charge C

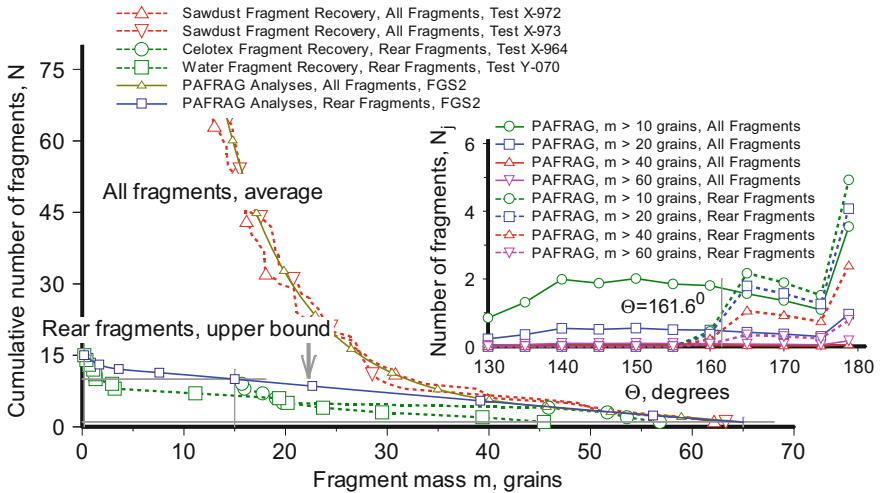


Fig. 15 Cumulative number of fragments versus fragment mass and number of fragments versus θ , for total “all fragments” and “rear only” ($\theta > 161.6^\circ$) distributions. Charge C

As shown in Fig. 14, Charge C PAFRAG modeling predicts that the majority of the munition’s fragment spray is projected into a relatively narrow θ -zone in the direction perpendicular to the projectile’s axis, approximately at angles $80^\circ \leq \theta \leq 100^\circ$. This is in good agreement with the flash radiography data showing no fragments projected to the projectile’s anterior region, $0^\circ \leq \theta \leq 50^\circ$. The

fragment velocity “spikes” in the region of $0^\circ \leq \Theta \leq 50^\circ$ (see fragment velocity plot, Fig. 13), are due the numerical “noise” from a few “stray” mix-material computational cells from the CALE modeling. Because there is no considerable fragment mass in the front Θ -zones, the overall effect of these errors is negligible, and the “average” fragment velocity in the $0^\circ \leq \Theta \leq 50^\circ$ region should be disregarded.

As evidenced from the flash radiographic images presented in Fig. 14, the tracer holder portion of the warhead breaks up into a number of relatively large fragments projected in the negative z -axis direction, back towards the gunner. As shown in Fig. 14, in excellent agreement with the Celotex™ and the water test fragment recovery data, PAFRAG modeling predicts that approximately 7.2% of the total fragment mass is projected to the “rear”, in the region of $161.6^\circ \leq \Theta \leq 180^\circ$. Since according to PAFRAG modeling and the flash radiography data, Fig. 13, the velocities of these fragments is approximately 0.05 cm/ μ s, the broke-up pieces of the projectile’s tracer holder are capable of causing serious injuries or death to the gunner.

Figure 15 shows PAFRAG-FGS2 model predictions of the cumulative number of fragments versus fragment mass, $N = N(m)$, and of the Θ -zonal number of fragments versus Θ , $N_j = N_j(\Theta)$, for both the total “all fragments” and the “rear only” ($161.6^\circ \leq \Theta \leq 180^\circ$) modeling cases. The “all fragments” fragment distribution was assessed from the sawdust fragment recovery tests that included fragments from the tracer section together with all fragments from the entire shell. The “rear only” fragment distribution was obtained from the Celotex™ and from the water test fragment recovery experimentation and accounted only for fragments projected at angles greater than approximately 161.6° . The limiting rear fragment collection angle of $\Theta = 161.6^\circ$ represents the altitudinal angle Θ covering the fragment recovery surface area.

As shown in Fig. 15, the “rear fragments” PAFRAG-FGS2 model fragment distribution was obtained by fitting Eq. (5) to the upper bound of the Celotex™ and water test recovery data, providing an additional “safety” margin for the safe separation distance analyses. Since in a typical fragmentation warhead only a few fragments are projected backward towards the gunner, establishing a statistically robust data base from the conventional fragmentation arena test requires repeated experimentation and is expensive. In contrast, the data from the PAFRAG modeling offers to munition designers more warhead performance information for significantly less money spent. The PAFRAG provides more detailed and more statistically accurate warhead fragmentation data for ammunition safe separation distance analysis, as compared to the traditional fragmentation arena testing approach.

8 Charge C PAFRAG Model Analyses: Assessment of Lethality and Safety Separation Distance

The safety separation distance analyses presented in this work were performed employing the JMEM/OSU Lethal Area Safety Program for Full Spray Fragmenting Munitions code [43] and the Wedge model computational module. According to Ref. [44], the safe separation distance is defined as fixed distance from the weapon’s launch platform and personnel beyond which functioning of the munition presents an acceptable risk of a hazard to the personnel and the platform. Accordingly, the safe separation hazard probability had been calculated based on the warhead’s fragment spray ability to strike and to penetrate exposed (bare) skin tissue of unprotected gun crew personnel. According to the Ref. [44], the maximum total risk to the munition crew at safe separation distance is generally accepted as 10^{-6} .

The input for the lethality and safe separation distance analyses included a range of possible ballistic projectile trajectories and the static PAFRAG FGS2 model predictions of the fragment spray blast characteristics. Figure 16 shows resulting plots of areas with $0.1 \leq P_i \leq 1$ and $P_i \leq 10^{-6}$ unprotected personnel risk hazards for varying projectile launch velocities. As shown in Fig. 16, the projectile launch velocity has a significant effect on both the munition lethality ($0.1 \leq P_i \leq 1$) and the safety ($P_i \leq 10^{-6}$). As shown in the figure, if the gun operates normally and launches the projectile with the nominal muzzle velocity of V_0 , all fragments are projected in the forward direction, posing no danger to the gun crew. However, if the gun misfires ($V_z \ll V_0$) and the munition is detonated, the results may be catastrophic.

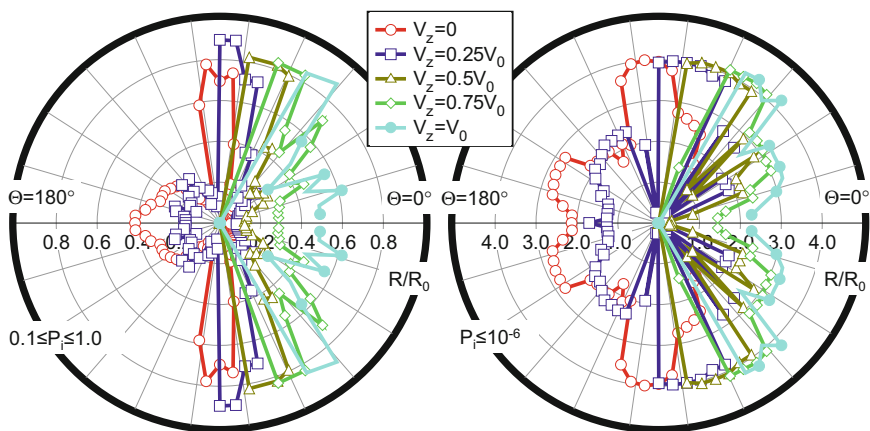


Fig. 16 Cumulative number of fragments versus fragment mass and number of fragments versus θ , for total “all fragments” and “rear only” ($\theta > 161.6^\circ$) distributions. Charge C

9 Summary

The fundamental vision of the US Army Armaments Research, Design and Engineering Center, Picatinny Arsenal is that the fragmentation ammunition has to be safe for the soldier and lethal for the adversaries. PAFRAG (Picatinny Arsenal FRAGMENTation) is a combined analytical and experimental technique for determining explosive fragmentation ammunition lethality and safe separation distance without costly arena fragmentation tests. PAFRAG methodology integrates high-strain high-strain-rate computer modelling with semi-empirical analytical fragmentation modelling and experimentation, offering warhead designers and ammunition developers more ammunition performance information for less money spent. PAFRAG modelling and experimentation approach provides more detailed and accurate warhead fragmentation data for ammunition safe separation distance analysis, as compared to the traditional fragmentation arena testing approach.

Acknowledgements The author wishes to express his gratitude to Dr. E.L. Baker of US Army ARDEC for many enjoyable and valuable discussions, for his initiative, leadership, and invaluable support, for all that made this PAFRAG work possible. Dr. B.E. Fuchs is acknowledged for his original contributions in development of PAFRAG experimentation. Messrs. W.J. Poulos, G.I. Gillen, and E.M. Van De Wal, all of US Army ARDEC, are acknowledged for their contributions in planning and conducting PAFRAG experiments. Messrs. K.W. Ng and J.M. Pincay, and Mrs. Y. Wu, all of US Army ARDEC, are acknowledged for their contributions in preparing CALE models employed in analyses. Mr. T. Fargus and Mrs. D.L. Snyder of US Army ARDEC are acknowledged for performing lethality and safety separation distance analyses. Messrs. K. P. Ko of PM MAS, A.N. Cohen, G.C. Fleming, J.M. Hirlinger, and Mr. G.S. Moshier, all of US Army ARDEC are acknowledged for providing funds that made this work possible.

References

1. Gurney RW (1943) The initial velocities of fragments from shells, bombs, and grenades. US Army Ballistic Research Laboratory Report BRL 405, Aberdeen Proving Ground, Maryland, Sept 1943
2. Mott NF (1943) A theory of fragmentation of shells and bombs. Ministry of Supply, A.C. 4035, May 1943
3. Taylor GI (1963) The fragmentation of tubular bombs, paper written for the Advisory Council on Scientific Research and Technical Development, Ministry of Supply (1944). In: Batchelor GK (ed) The scientific papers of Sir Geoffrey Ingram Taylor, vol 3. Cambridge University Press, Cambridge, pp 387–390
4. Gurney RW, Sarmousakis JN (1943) The mass distribution of fragments from bombs, shell, and grenades. US Army Ballistic Research Laboratory Report BRL 448, Aberdeen Proving Ground, Maryland, Feb 1943
5. Hekker LJ, Pasman HJ (1976) Statistics applied to natural fragmenting warheads. In: Proceedings of the second international symposium on ballistics, Daytona Beach, Florida, 1976, p 311–24
6. Grady DE (1981) Fragmentation of solids under impulsive stress loading. *J Geophys Res* 86:1047–1054

7. Grady DE (1981) Application of survival statistics to the impulsive fragmentation of ductile rings. In: Meyers MA, Murr LE (eds) Shock waves and high-strain-rate phenomena in metals. Plenum Press, New York, pp 181–192
8. Grady DE, Kipp ME (1985) Mechanisms of dynamic fragmentation: factors covering fragment size. *Mech Mat* 4:311–320
9. Grady DE, Kipp ME (1993) Dynamic fracture and fragmentation. In: Asay JA, Shahinpoor M (eds) High-pressure shock compression of solids. Springer, New York, pp 265–322
10. Grady DE, Passman SL (1990) Stability and fragmentation of ejecta in hypervelocity impact. *Int J Impact Eng* 10:197–212
11. Kipp ME, Grady DE, Swegle JW (1993) Experimental and numerical studies of high-velocity impact fragmentation. *Int J Impact Engng* 14:427–438
12. Grady DE (1987) Fragmentation of rapidly expanding jets and sheets. *Int J Impact Eng* 5:285–292
13. Grady DE, Benson DA (1983) Fragmentation of metal rings by electromagnetic loading. *Exp Mech* 4:393–400
14. Grady DE (1988) Spall strength of condensed matter. *J Mech Phys Solids* 36:353–384
15. Grady DE, Dunn JE, Wise JL, Passman SL (1990) Analysis of prompt fragmentation Sandia report SAND90-2015, Albuquerque. Sandia National Laboratory, New Mexico
16. Grady DE, Kipp ME (1980) Continuum modeling of explosive fracture in oil shale. *Int J Rock Mech Min Sci Geomech Abstr* 17:147–157
17. Hoggatt CR, Recht RF (1968) Fracture behavior of tubular bombs. *J Appl Phys* 39:1856–1862
18. Wesenberg DL, Sagartz MJ (1977) Dynamic fracture of 6061-T6 aluminum cylinders. *J Appl Mech* 44:643–646
19. Grady DE (2005) Fragmentation of rings and shells. The legacy of N.F. Mott. Springer, Berlin
20. Mercier S, Molinari A (2004) Analysis of multiple necking in rings under rapid radial expansion. *Int J Impact Engng* 30:403–419
21. Weiss HK (1952) Methods for computing effectiveness fragmentation weapons against targets on the ground. US Army Ballistic Research Laboratory Report BRL 800, Aberdeen Proving Ground, Maryland, Jan 1952
22. Grady DE (1990) Natural fragmentation of conventional warheads. Sandia Report No. SAND90-0254. Sandia National Laboratory, Albuquerque, New Mexico
23. Vogler TJ, Thornhill TF, Reinhart WD, Chhabildas LC, Grady DE, Wilson LT et al (2003) Fragmentation of materials in expanding tube experiments. *Int J Impact Eng* 29:735–746
24. Goto DM, Becker R, Orzechowski TJ, Springer HK, Sunwoo AJ, Syn CK (2008) Investigation of the fracture and fragmentation of explosive driven rings and cylinders. *Int J Impact Eng* 35:1547–1556
25. Wang P (2010) Modeling material responses by arbitrary Lagrangian Eulerian formulation and adaptive mesh refinement method. *J Comp Phys* 229:1573–1599
26. Moxnes JF, Prytz AK, Froland Ø, Klokkehaug S, Skriudalen S, Friis E, Teland JA, Dorum C, Ødegardstuen G (2014) Experimental and numerical study of the fragmentation of expanding warhead casings by using different numerical codes and solution techniques. *Defence Technol* 10:161–176
27. Demmie PN, Preece DS, Silling SA (2007) Warhead fragmentation modeling with Peridynamics. In: Proceedings 23rd international symposium on ballistics, pp 95–102, Tarragona, Spain, 16–20 Apr 2007
28. Wilson LT, Reedal DR, Kipp ME, Martinez RR, Grady DE (2001) Comparison of calculated and experimental results of fragmenting cylinder experiments. In: Staudhammer KP, Murr LE, Meyers MA (eds) Fundamental issues and applications shock-wave and high-strain-rate phenomena. Elsevier Science Ltd., p 561–569
29. Bell RR, Elrick MG, Hertel ES, Kerley GI, Kmetyk LN, McGlaun JM et al (1992) CTH code development team. CTH user's manual and input instructions, Version 1.026. Sandia National Laboratory, Albuquerque, New Mexico, Dec 1992

30. Kipp ME, Grady DE (1985) Dynamic fracture growth and interaction in one-dimension. *J Mech Phys Solids* 33:339–415
31. Tipton RE (1991a) CALE User's manual, Version 910201. Lawrence Livermore National Laboratory
32. Baker EL (1991) An explosive products thermodynamic equation of state appropriate for material acceleration and overdriven detonation. Technical Report AR-AED-TR-91013. Picatinny Arsenal, New Jersey
33. Baker EL, Stiel LI (1998) Optimized JCZ3 procedures for the detonation properties of explosives. In: Proceedings of the 11th international symposium on detonation. Snowmass, Colorado; August 1998, p 1073
34. Stiel LI, Gold VM, Baker EL (1993) Analysis of Hugoniot and detonation properties of explosives. In: Proceedings of the tenth international symposium on detonation. Boston, Mass, July 1993, p 433
35. Steinberg DJ, Cochran SG, Guinan MW (1980) A constitutive model for metals applicable at high-strain rate. *J Appl Phys* 51:1498–1504
36. Tipton RE (1991b) EOS coefficients for the CALE-code for some materials. Lawrence Livermore National Laboratory
37. Steinberg DJ (1996) Equation of state and strength properties of selected materials. Technical Report UCRL-MA-106439. Lawrence Livermore National Laboratory, Livermore, California
38. Joint Munition Effectiveness Manual (1989) Testing and data reduction procedures for high-explosive munitions. Report FM 101-51-3, Revision 2, 8 May 1989
39. Mott NF (1947) F.R.S., Fragmentation of steel cases. *Proc Roy Soc* 189:300–308
40. Ferguson JC (1963) Multivariable curve interpolation. Report No. D2-22504, The Boeing Co., Seattle, Washington
41. Pearson J. A fragmentation model for cylindrical warheads. Technical Report NWC TP 7124, China Lake, California: Naval Weapons Center; December 1990
42. Mock W Jr, Holt WH (1983) Fragmentation behavior of Armco iron and HF-1 steel explosive-filled cylinders. *J Appl Phys* 54:2344–2351
43. Joint Technical Coordination Group for Munitions Effectiveness (1991) Computer program for general full spray materiel MAE computations. Report 61 JTCG/ME-70-6-1, 20 Dec 1976, Change 1: 1 Apr 1991
44. (1999) Guidance for Army Fuze Safety Review Board safety Characterization. US Army Fuze Office, Jan 1999
45. Griffith AA (1920) The phenomena of rapture and flow in solids. *Phil Trans Royal Soc Lond* A221:163
46. Griffith AA (1924) The theory of rapture. In: Biezeno CB, Burgurs JM, Waltman Jr J (eds) Proceedings of the first international congress of applied mech, Delft, p 55
47. Mott NF, Linfoot EH (1943) A theory of fragmentation. Ministry of Supply, A.C. 3348, Jan 1943